



Cite this: RSC Adv., 2017, 7, 34736

A study of the 160 MeV Ni^{7+} swift heavy ion irradiation effect of defect creation and shifting of the phonon modes on $\text{Mn}_x\text{Zn}_{1-x}\text{O}$ thin films[†]

H. A. Khawal and B. N. Dole  *

$\text{Mn}_x\text{Zn}_{1-x}\text{O}$ thin films were successfully synthesized by the dip coating technique. The thin films were irradiated by Ni^{7+} swift heavy ions (SHI) with 1×10^{13} ions per cm^2 fluence, and their structural, electrical, Raman spectral and surface morphological properties were investigated. X-ray diffraction patterns confirmed the $P6_3mc$ space groups, and the crystallite size increased after SHI irradiation, due to electron rearrangements. *I*–*V* studies revealed enhanced conductivity after Ni^{7+} SHI irradiation and showed the ohmic nature of the sample. The irradiation sensor efficiency and responsibility were calculated by using *I*–*V* data, which revealed impressive results. Photoluminescence (PL) measurements were performed to determine the evolution of defects and defect-annealing during ion irradiation; enhancement in the luminosity of pure and 5% Mn substituted ZnO thin films was observed. The presence of the Raman active strongest optical phonon mode of ZnO at 436.19 cm^{-1} revealed that ZnO with hexagonal wurtzite structure supported the XRD results. Atomic force microscopy (AFM) images revealed the formation of nano-bunches on the surface and enhanced the surface roughness and skewness of the irradiated samples, due to coulombic interactions between electrons and ions.

Received 13th February 2017
 Accepted 19th June 2017

DOI: 10.1039/c7ra01809f
rsc.li/rsc-advances

Introduction

Nanotechnology is an interdisciplinary research field with vast applications in materials technology, manufacturing, instrumentation, energy production and storage, information technology, chemical technology and the medical field.^{1–3} However, there are many issues to be addressed, including toxicity and the environmental impact of nanostructured materials and their potential effects on global economies. The many applications of ZnO nanomaterials in spintronic devices, such as optical isolators, spin-valve transistors, non-volatile memory, ultra-fast optical switches and spin-light emitting diodes, inspire extensive research work to synthesize diluted magnetic semiconductors (DMS) with III–V and II–VI semiconductors.^{4–12} Among the different types of semiconducting nanomaterials, zinc oxide (ZnO) is one of the significant multifunctional materials that finds applications in the various fields. ZnO is cheap in cost and is environmentally friendly as compared to other materials.¹³ Normally, ZnO is studied on the nanoscale; this is probably because the high surface area to volume ratio of

nanoparticles could increase the adsorption of organic pollutants on the surface of the particles, as compared to bulk materials.^{14–23} ZnO belongs to the group II–VI binary compound semiconductors; in the hexagonal structure it is an n-type semiconductor with high electron mobility, a direct energy bandgap of 3.37 eV and a high exciton binding energy of 60 meV, which is greater than the thermal energy at room temperature. Due to the excellent structural, electrical, optical and morphological properties, ZnO thin films have wide applications as solar cells²⁴ gas sensors,^{25,26} light emitting diodes (LED's)²⁷ and transparent electrodes.²⁸ Moreover, they can be prepared by different techniques, such as pulsed laser deposition,²⁹ the dip coating method,³⁰ chemical vapor deposition,³¹ magnetron sputtering,³² the spin coating method,³² atomic layer deposition,³³ and thermal evaporation.³⁴ Among the above methods to prepare ZnO , the dip coating method is extremely attractive, due to its features such as its simplicity, low temperature, low cost, easy coating of large surfaces and low evaporation temperature.

It is well known that doping a selective element into ZnO has become an important route to improving the structural, electrical, morphological, optical, and magnetic properties, and increasing the carrier concentration for electronic applications because a higher carrier concentration is required. Recently, many studies have been focused on the transition metals (TM) such as Mn, Ni, Fe, Co and Cr doped into ZnO , due to their potential applications in spintronics.³⁵

Advanced Materials Research Laboratory, Department of Physics, Dr Babasaheb Ambedkar Marathwada University, Aurangabad-431 004, India. E-mail: drbndole.phy@gmail.com

† Electronic supplementary information (ESI) available: Ion collision, ion recoil distribution, energy loss of target phonon and energy loss of vacancy production plots are shown in Fig. 1. Table 1 shows the lattice binding energy, surface binding energy and displacement energy of ZnO nanoparticles are calculated by TRIM software. See DOI: [10.1039/c7ra01809f](https://doi.org/10.1039/c7ra01809f)



Swift heavy ions (SHI) are particle radiations accelerated to very high energies, typically in the MeV or GeV range, having sufficient mass and energy to penetrate solid materials. Irradiation with GeV energy ions has been found to produce intermixing in the Fe/Si multilayer (Bauer *et al.* 1993).³⁶ It was shown by Dunlop *et al.* (1994)³⁷ that trails of damage can be made in metals by high levels of electronic energy loss, S_e . Threshold S_e for such columnar damage varies from metal to metal, for example, S_e for Fe is ~ 5 keV \AA^{-1} (Dunlop *et al.* 1994). Recently, researchers have shown interest in atomic mixing, materials modification and phase changes using ion beam mixing of high energy, where inelastic collisions or electronic stopping are responsible for the energy loss. Veenu Sisodia and Jain (2004)³⁸ studied mixing induced by swift heavy ion irradiation at Fe/Si interfaces. To date, tubular Mn-doped ZnO structures grown by the solution method have seldom been reported.

In this paper, we propose a new and facile chemical solution method to synthesize the hexagonal Mn-doped ZnO thin films on a large scale, *via* a dip coating technique. The effect of SHI irradiation on the structural, electrical, morphological and photoluminescence properties of Mn doped ZnO thin films are presented.

Experimental procedure

Synthesis of thin films

Thin films of pure and Mn substituted ZnO, using glass substrates, were synthesized by the dip coating technique that was fully based on the adsorption and reaction of the ions from the solutions. The fundamental building block of the dip coating technique is the collection of samples on the surface of another substance.

The pure ZnO thin film was obtained from 0.1 M zinc chloride solution, dissolved in 40 mL distilled water with constant stirring for 1 h at room temperature. Sodium hydroxide (NaOH, 0.1 M) solution was dissolved in 40 mL distilled water for 1 h at 70 °C in a separate beaker. A zincket bath was prepared by adding 2–3 drops of triethanolamine (TEA) and 5–6 drops of ammonia in zinc chloride solution for maintaining the pH at 11. The sodium hydroxide solution was added to the zincket bath and stirred at 80 °C for 1 h using magnetic stirrer. A glass substrate was immersed in hydrochloric acid for 24 h and was subsequently cleaned ultrasonically with acetone and distilled water, and dried on a hot plate at 75 °C for 1 h. The cleaned substrate was dipped in the solution for 30 minutes (three cycles, 10 minute gap) at 80 °C. The film deposited was then dried in air for 60 minutes at 250 °C.

Similarly, for the synthesis of Mn doped ZnO thin films, three solutions, 0.1 M of zinc chloride, 0.1 M of manganese chloride (MnCl_2) and NaOH, were separately dissolved in 40 mL of distilled water. NaOH solution was stirred at 70 °C for 1 h; 0.1 M of zinc chloride solution, and 0.1 M of manganese chloride (MnCl_2) solution were stirred at room temperature for 1 h, using a magnetic stirrer, then 5% of manganese MnCl_2 solution was added into the zinc chloride solution with constant stirring at room temperature. TEA (2 drops) and 5–6 drops of ammonia were added to the zinc chloride solution for preparation of the

zincket bath. NaOH solution was added to the zincket bath and stirred at 80 °C for 1 h. The cleaned substrate was dipped in the solution for 30 minutes (10 minute gap, three cycles) at 80 °C. The film was deposited then dried in air for 60 minutes at 250 °C. The manganese concentration was varied up to 5% for the preparation of Mn doped ZnO thin films.

Irradiation experiment

The thin film samples were mounted on an electrically insulated sample ladder and the ladder current was integrated to collect and count the charge pulses *via* a scalar counter, along with the digital current integrator. The pure and Mn doped ZnO films were irradiated with 160 MeV Ni^{7+} ions, at room temperature, with fluence of 1×10^{13} ions per cm^2 , using a 15 UD Pelletron accelerator at the Inter-University Accelerator Centre (IUAC), New Delhi, India. The beam current was maintained at 1 pA (particle nanoampere). This was kept low in order to prevent the sample from heating up during irradiation. The beam was raster scanned over an area of $1 \times 1 \text{ cm}^2$, using a magnetic scanner. The damage caused by the interaction between the ion beam and target material was calculated using the SRIM software. The electronic stopping power (S_e) and nuclear stopping power (S_n) of the 160 MeV Ni^{7+} ions for pure and Mn doped ZnO films were calculated using SRIM-2008. The range of the projectile ions of Ni^{7+} for 160 MeV electronic energy loss was 1.033×10^3 keV μm^{-1} and nuclear energy loss was 1.42 keV μm^{-1} and the range was 20.88 μm ; ion collision was calculated by depth *versus* Y axis plot, shown in Fig. 1(a). It was

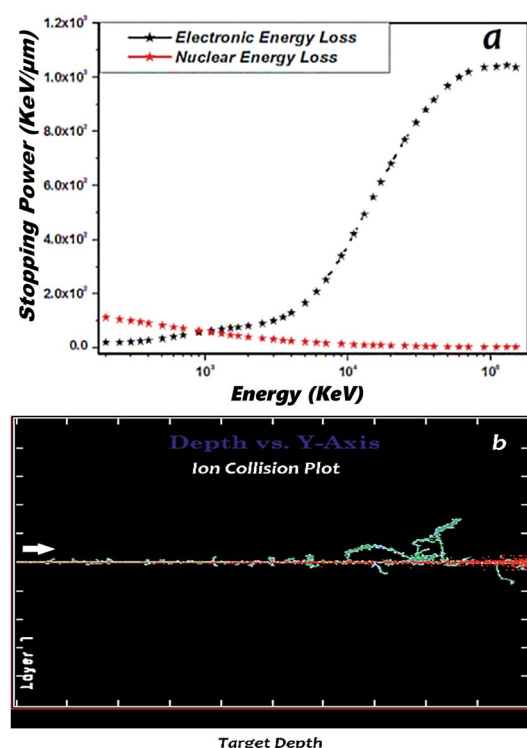


Fig. 1 (a) Simulated electronic and nuclear energy loss in the 160 MeV Ni^{7+} SHI irradiation of ZnO. (b) Ion collision effect of SHI irradiation.



found that the energy loss to target phonons consisted of the direct creation of phonons by the ion and the additional energy loss by target recoil atoms to phonons, as shown in Fig. 1(b).

Detailed information for the Li^{3+} SHI irradiation effect on pure and Mn doped ZnO samples of ion collision, ion recoil distribution, the energy loss of target phonon and energy loss of vacancy production plots can be found in (ESI†).

Material characterization

The pristine and irradiated films were characterized using different techniques. The structural properties were investigated by XRD studies, and patterns were recorded using a D-8 Advance X-ray diffractometer (acquired from Bruker AXS Germany) with the monochromatic $\text{CuK}\alpha$ conventional X-ray source, Göbble mirror, LiF monochromator, scintillator detector. I - V measurements were taken at IUAC, New Delhi. Raman spectra of pure and Mn doped ZnO samples were recorded by using an Ar ion laser with 514.5 nm wavelength and 50 mW power as the excitation source. Surface morphologies were studied by atomic force microscopy (AFM) in the tapping mode with an antimony-doped silicon tip, using a Nanoscope.

Results and discussion

Crystallographic analysis

X-ray diffraction patterns were used to investigate the crystallographic structure of the as-synthesized samples. The X-ray diffraction patterns were obtained for pristine and $\text{Zn}_{1-x}\text{Mn}_x\text{O}$ with nominal composition ($x = 0.05$) irradiated with SHI Ni^{7+} ions. The X-ray diffraction patterns of the pristine and irradiated, pure and 5% Mn doped ZnO thin films are shown in Fig. 3. The patterns show strong and sharp diffraction peaks, demonstrating good crystallinity, and are matched with the common ZnO hexagonal phase, *i.e.*, the wurtzite structure [80-0074, JCPDS]. These peaks, at angles (2θ) of 31.89° , 34.43° , 36.33° , 47.63° , 56.73° and 62.96° , correspond to the diffractions from the (100), (002), (101), (102), (110) and (103) planes. Pure

and 5% Mn doped ZnO samples usually have decreased intensity after SHI irradiation, as reported by S. K. Neogi *et al.*,³⁹ but in our case, it was observed that the increase in intensity accounted for the influence of ions on the scattering factors of the unit cell. Enhancement in the intensity may also be due to changes in the electronic density in the crystallographic position and the increase in peak intensity is an indication of the improvement of the crystallinity of the samples. The absence of the diffraction peaks of manganese oxide (Mn) structures in the XRD pattern may imply Mn incorporation within the ZnO thin films by means of substitution for Zn, or that the content of the manganese impurities is lower than the limitation of the XRD. The lattice parameters for hexagonal Mn doped ZnO thin films were calculated from the (102) plane. Lattice parameters (a and c) were calculated from XRD data using eqn (1).⁴⁰

$$\frac{1}{d^2} = \frac{4}{3} \frac{[h^2 + hk + k^2]}{a^2} + \frac{l^2}{c^2} \quad (1)$$

where ' a ' and ' c ' are the lattice parameters and (hkl) are the Miller indices, d is the interplanar spacing for the plane (hkl) . It can be seen from Table 1 that the values of the lattice constants,

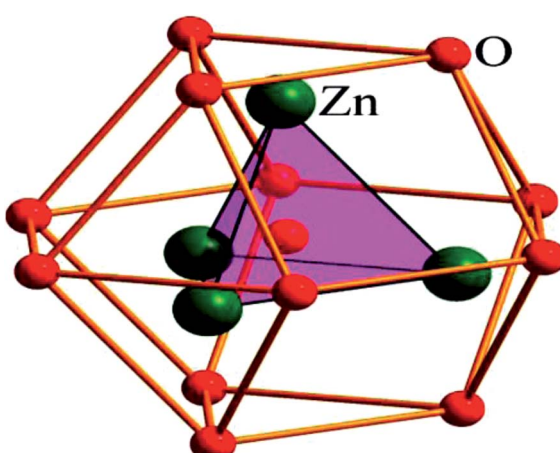


Fig. 2 Creation of voids in Mn doped ZnO samples after SHI irradiation.

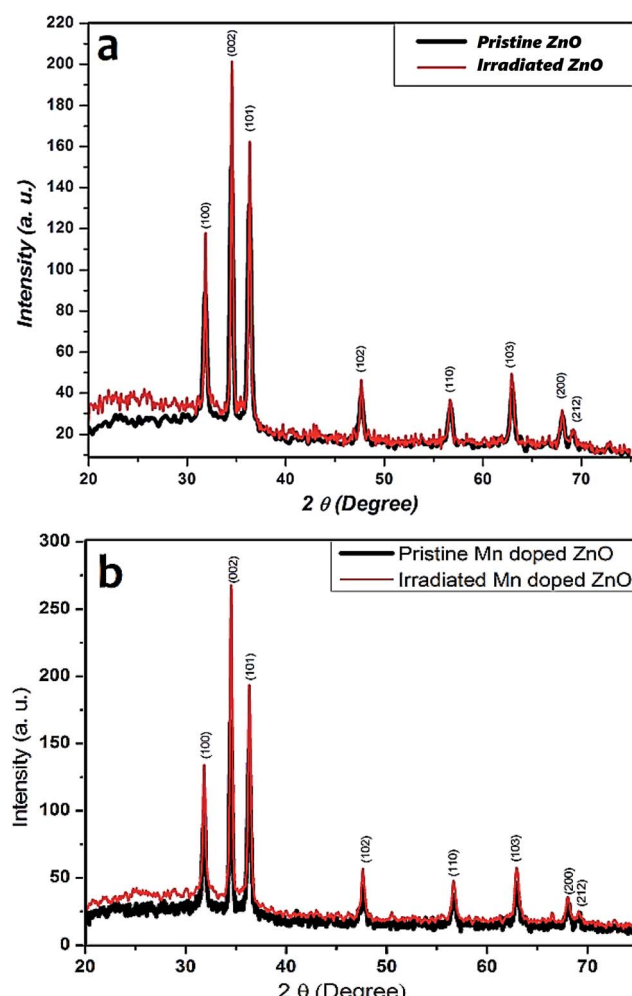


Fig. 3 XRD patterns of (a) pristine and irradiated ZnO, (b) pristine and irradiated 5% Mn doped ZnO thin films.



for pure and Mn doped ZnO, and pristine and SHI irradiated thin films, decrease the lattice parameters after SHI irradiation as well as increase Mn concentration. The decrement in the lattice parameters with dopant concentration and irradiation of the crystal can be understood as a phase transition or the actual incorporation of dopant into the unit cell of the host structure. This decrement in lattice parameters with dopant concentration can be explained by Vegard's rule. This rule holds that a linear relation exists at a constant temperature, between the crystal lattice constant of an alloy and the concentration of the constituent elements.⁴¹

The crystallite sizes of pure and Mn doped ZnO, pristine and irradiated thin films were calculated using the Debye–Schererrer formula:⁴²

$$D = \frac{0.9\lambda}{\beta \cos \theta} \quad (2)$$

where D is the crystallite size, λ is the wavelength with CuK_α radiation (1.5406 Å), β is the full width at half maximum and θ is the Bragg's angle of diffraction. After SHI irradiation, the crystallite size was decreased as reported by S. Som *et al.*,⁴³ but in our case, it was observed that there was an increase in crystallite size with increasing Mn content in the samples, and it was also observed that after SHI irradiation, there was an increase in the crystallite size as compared to the pristine sample. This might be due to the stress released between the grains and the decrease in the concentration of oxygen vacancies at a fluence of 1×10^{13} ions per cm^2 .

The dislocation density was calculated as the amount of defects in the crystal, or the irregularity within a crystal structure. Dislocations are a type of topological defect. The movement of a dislocation is impeded by other dislocations present in the sample; thus, a larger dislocation density implies a greater hardness. The dislocation density represents the magnitude of defects in the film. The dislocation density was calculated by using the following formula:⁴⁴

$$\delta = \frac{1}{D^2} \quad (3)$$

where D is the crystallite size of the samples. The values of dislocation density (δ) for pure, pristine ZnO is 1.972×10^{-3} (nm)⁻², and is 1.467×10^{-3} (nm)⁻² upon irradiation with fluence of 1×10^{13} ions per cm^2 . The same trend was observed in Mn doped ZnO thin films; a decrease in dislocation density with increasing Mn concentration as well as SHI irradiation was

observed. The values of dislocation density decreased with increasing fluence, as summarized in Table 1. This clearly implies that the enhancement of defects in the samples is due to the formation of more wide cylindrical ion tracks after irradiation with Ni^{7+} ions on Mn doped ZnO samples.

The X-ray density ' P_x ' was calculated using the known formula:⁴⁵

$$P_x = \frac{nM}{N_A V} \quad (4)$$

where n is the number of atoms per unit cell, M is the molecular weight of the samples, N_A is Avogadro's number and V is the volume of the unit cell. It was found that the X-ray density decreases with increasing Mn concentration and also increases after SHI irradiation, clearly implying that the effect of irradiation on the density of the sample was decreased. This may be due to the larger ionic radius of Mn ions, compared to Zn ions.

The atomic packing factor (APF) is the fraction of volume in a crystal structure that is occupied by atoms. It is dimensionless and is always less than unity. Pure and Mn doped ZnO nanoparticles have the wurtzite structure, with HCP (hexagonal close-packed) arrangement. HCP has two types of voids in the crystal structure, *i.e.* tetrahedral and octahedral voids.

After SHI irradiation of pure and Mn doped ZnO, the values of APF were reduced with Ni^{7+} ions irradiation, which introduced the presence of voids. Reshak *et al.*⁴⁶ reported that the space group of the ZnO sample is $P6_3mc$ for this structure, which has six octahedral voids in the 2a sites with coordinate (0 0 3/4) geometry. The shortest distance between the oxygen atoms from the octahedral voids is 2.28 Å, as shown in Fig. 2.

The APF of the materials was evaluated using the following formula:⁴⁷

$$\text{APF} = \frac{2\pi a}{3\sqrt{3}c} \quad (5)$$

It was observed that the value of APF slightly decreased after SHI irradiation, which may be due to the enhancement of voids in the samples. The APF of bulk hexagonal ZnO materials is about 74%, but in our case, the APF of ZnO nanoparticles is nearly 75% for the pristine sample, and is 74.5% for the irradiated sample, in a hexagonal structure. This means that the APF in nanocrystals is slightly larger than that of bulk materials, due to the effect of SHI irradiation on the samples.

Table 1 Lattice parameters, crystallite size, APF, X-ray density and surface to volume ratio of pristine and irradiated, pure and Mn substituted ZnO thin films at fluence of 5×10^{13} ions per cm^2

Sample	Fluence (ions per cm^2)	Lattice parameter		Crystallite size (nm)	APF	X-ray density (gm cm^{-3})	S/V
		a (nm)	c (nm)				
$x = 0.00$	Pristine	0.3271	0.5215	23.57	0.767	5.691	0.050
	Irradiated 5×10^{13} ions per cm^2	0.3268	0.5209	24.41	0.761	5.638	0.043
$x = 0.05$	Pristine	0.3269	0.5206	27.64	0.758	5.699	0.039
	Irradiated 5×10^{13} ions per cm^2	0.3253	0.5156	32.24	0.757	5.596	0.029



The surface area to volume ratio of the nanoparticles has a significant effect on their properties. Firstly, thin films have a relatively larger surface area when compared to the same volume of the material. The surface to volume ratio was calculated by using the following equation:⁴⁸

$$\frac{\text{Surface}}{\text{Volume}} = \frac{SR_0}{V - SR_0} = \frac{3R_0}{R - SR_0} \quad (6)$$

where S is the surface area, V is the volume, R_0 is the ZnO distance (0.18 nm) and R is the average particle radius. The surface area to volume ratio decreases with SHI irradiation of the pure and Mn doped ZnO thin films, due to the increase in the average crystallite size, which is due to this surface area to volume ratio decrease. The values for the S/V ratio are listed in Table 1.

Photoluminescence (PL) study

Photoluminescence is a sensitive method for examining the sample quality, especially its optical properties. Further information about the optical properties of pure and Mn doped ZnO can be obtained from PL spectra, in addition to information about the crystal modality, structural defects such as oxygen vacancy, Zn interstitials and surface properties of particles. ZnO is a strongly luminescent material that is used with several polymers. The PL spectral studies before and after SHI irradiation using nickel ion irradiation with a high energy beam of 160 MeV of undoped and 5% Mn doped ZnO thin films were recorded in the wavelength range of 400 to 900 nm. Fig. 4 shows the PL spectra of the composite formed with the glass substrate, with a peak around 3.25 eV, attributed to the band-edge excitonic transition of ZnO. A broad emission band covers the green-red spectral region from 500 nm to 750 nm. Y. Hao *et al.*⁴⁹ reported PL spectra with UV emission and defect-related blue emission, but in our case it was noticed that in the visible range for all samples, the green-red emission presents a much higher intensity than the blue, indicating that yellow light is predominant in the white light emission. In pure ZnO thin films, the irradiated sample has increased wavelength as compared to the pristine pure ZnO, and the same trend was observed in 5% Mn doped ZnO thin films. On performing Gaussian deconvolution of the PL spectra, it was observed that an intense, broad, green band at 506 nm appeared in the PL spectra, which can be attributed to deep level emission caused by impurities and structural defects inherent in pristine ZnO nanoparticles, such as oxygen vacancies, zinc interstitials, *etc.*, and there was a less intense blue emission near 506 nm, because of intrinsic defects such as oxygen and zinc interstitials.⁵⁰

Herein, for pristine ZnO the sample exhibits a UV emission peak at 464.40 nm and five defect peaks, which correspond to green emissions near 543 and 572 nm and an orange band at 630 nm, and red emission near 706.41 nm in the PL spectra with Gaussian fitting. The main peak at 602.83 nm could be ascribed to the transition occurring from Zn interstitials to the valence band, and it may be the result of the singly ionized oxygen vacancy.⁵¹

The ZnO sample irradiated with Ni^{7+} SHI ions had an enhancement in the wavelength, into the visible and infrared

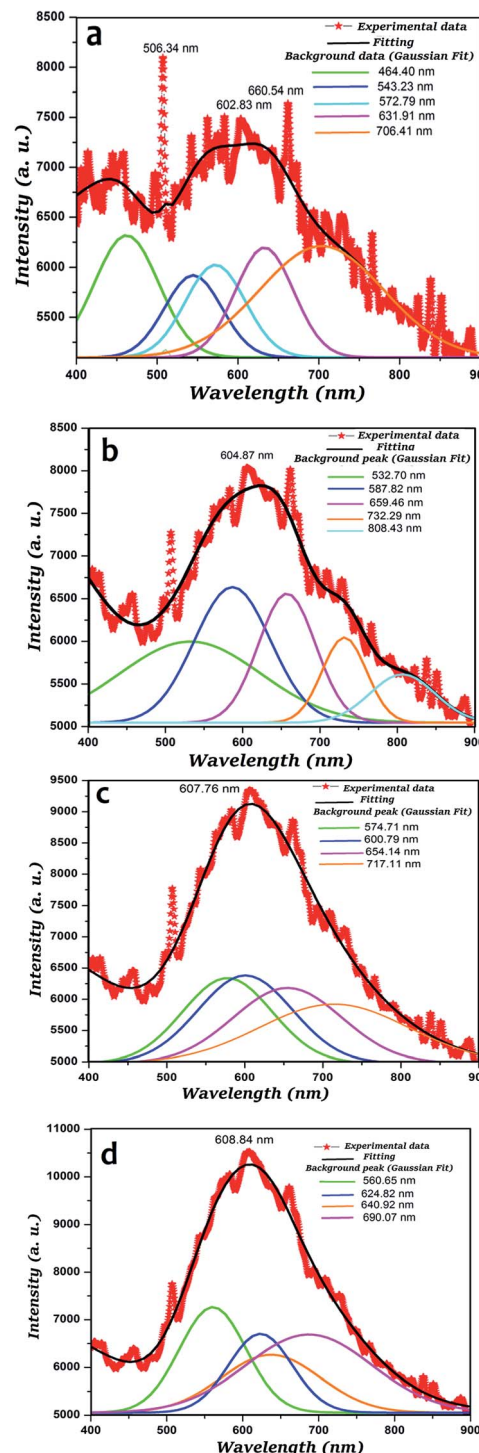


Fig. 4 PL spectra of (a) pristine ZnO thin film, (b) irradiated ZnO thin films, (c) pristine 5% Mn doped ZnO thin film, (d) irradiated 5% Mn doped ZnO thin films.

range for all spectra. Apart from the two common peaks, the other two emission peaks observed in the orange and the red regions are the focus of attention. The orange band at a wavelength of around 604.87 nm was attributed to either the presence of excess local oxygen or structural imperfections.⁵² Enhancement of the wavelength after SHI irradiation was due to



cascade formation in the inner core of the samples; this cascade changed the electron position and was observed in the infrared region. The fourth and fifth bands were Gaussian fitted, observed in the infrared region at wavelengths of 732.29 nm and 808.43 nm, respectively. The sputtered ZnO films exhibited n-type conductivity, which led to red and IR emission bands.⁵³ It is believed that this emission resulted from the formation of native defects. The origin of this band is still ambiguous and needs to be further investigated.

The 5% Mn doped ZnO sample had four peaks, at 574.71, 600.79, 654.14 and 717.11 nm, which were fit to the Gaussian model. Without irradiation, the spectra of the 5% Mn doped ZnO thin films were in the visible and infrared regions as compared to pure ZnO samples. It was observed that the enhancement of intensity as well as wavelength, are due to the effect of Mn doping in the ZnO. The peak at 607.76 nm, corresponding to the orange region, was enhanced as compared to the pure ZnO thin films; it is clearly evidenced that the Mn content increases the wavelength of the samples.

To perform Gaussian deconvolution of the PL spectra of Mn_xZn_{1-x} ($x = 0.05$) samples irradiated with Ni^{7+} SHI ions, the behavior of visible band components depending on x should be clarified. For this purpose, the PL spectra of the un-doped and Mn doped ZnO samples were measured under excitation by light with $\lambda = 320$ nm, corresponding to band-to-band absorption, and were analyzed. Four bands were observed, 560.65 nm, corresponding to green emission, 624.82 and 640 nm corresponding to orange emission and 690.07 nm corresponding to red emission. It is clear that the all spectra were observed the visible region, but after SHI irradiation, the intensity changed as well as the region of the band spectra, due to the cascade formation in the materials.

Raman spectra

The Raman spectra of pure and 5% Mn doped ZnO thin films in the range 200–800 cm^{-1} are shown in Fig. 5. The pure ZnO thin films have wurtzite structure with space symmetry C_{6v}^4 ($P6_3mc$), found using the Halford method.⁵⁴ The optical phonon irreducible representation is given by eqn (7).

$$\Gamma_{\text{opt}} = A_1 + 2B_1 + E_1 + 2E_2 \quad (7)$$

where A_1 and E_1 modes are polar and can split into transverse optical (TO) and longitudinal optical (LO) phonons, respectively; both are Raman active modes. The nonpolar E_2 mode is Raman active, while the B_1 mode is Raman inactive. Two formula units per primitive cell give six Raman active phonon modes at 101 (E_2 , low), 381 (A_1 , TO), 407 (E_1 , TO), 437 (E_2 , high), 554 (A_1 , LO), 583 cm^{-1} (E_1 , LO) and 776 (E_2 , high) of first order.⁵⁵ For pristine ZnO thin films, the four peaks that were observed are 333.05 cm^{-1} , 437.74 cm^{-1} , 574.55 cm^{-1} and 675.54 cm^{-1} . The broad peak at about 333.05 cm^{-1} , seen in the spectrum of pure ZnO, has been attributed to the second order Raman processes involving acoustic phonons. Second peak Raman mode at 437.74 cm^{-1} (E_2 , high) characteristic of ZnO and is mainly due to the vibration of the oxygen atoms in the ZnO lattice. Its presence demonstrates the good quality of the samples. The (E_1 , low) mode around 574

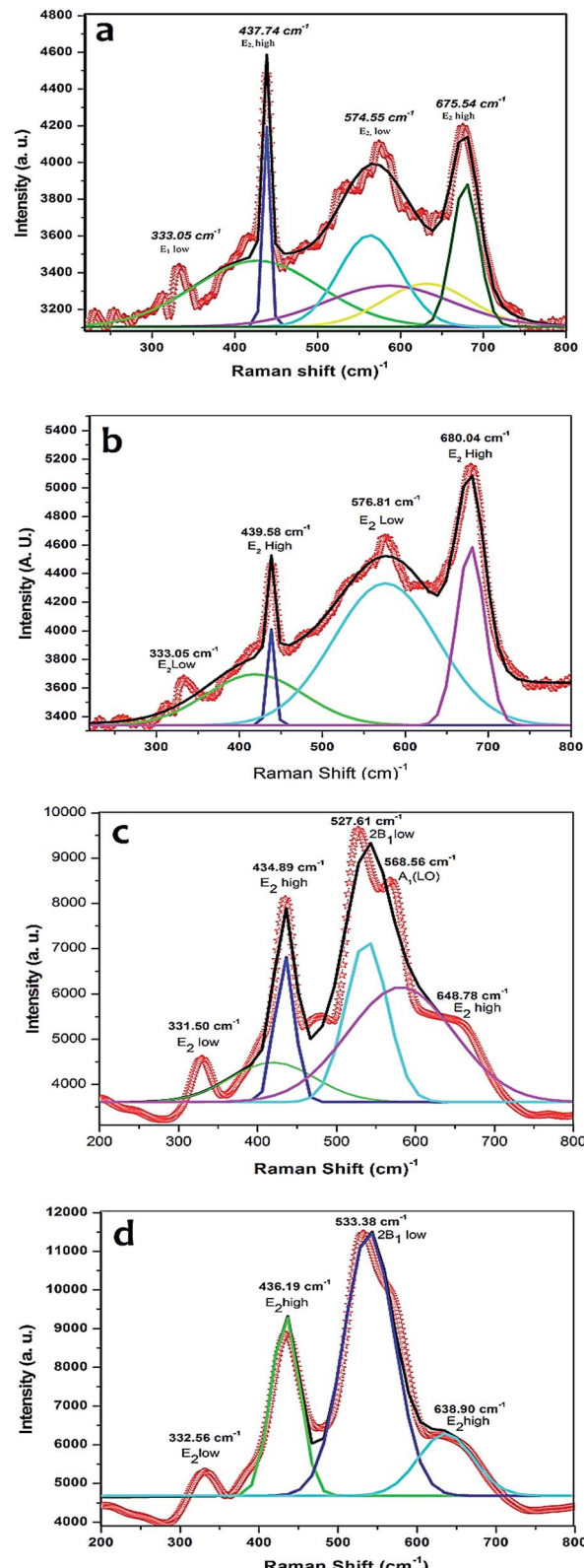


Fig. 5 The Raman spectra of (a) pristine ZnO, (b) irradiated ZnO, (c) pristine 5% Mn doped ZnO, (d) irradiated 5% Mn doped ZnO thin films.

cm^{-1} , according to Asokan *et al.*,⁵⁶ and 587–591 cm^{-1} , strictly speaking, cannot be observed in a backscattering geometry as a dipole-allowed mode.⁵⁷



In irradiated pure ZnO thin films, the four Raman modes, 333.05, 439.58, 576.81 and 680.04 cm^{-1} , were observed. The observed phonon mode is (E_2 , high) 436 cm^{-1} , shifted towards higher wave number, 439.58 cm^{-1} , with respect to pristine ZnO, as is usual for nanocrystals.⁵⁸ The spectra of the irradiated films show that the intensity of the E_2 high (680.04 cm^{-1}) mode increases drastically upon irradiation at $1 \times 10^{13} \text{ cm}^2$ fluence, due to the high energetic ions interacting with the electrons in the samples, due to the change in the geometry as well as the structure of the sample.

Mn doped ZnO pristine samples showed peaks, in the Gaussian fitted mode, at 331.50, 434.89, 527.61 and 568.56 cm^{-1} . The peak wavelength decreases of Mn doped ZnO samples as compared to the pure ZnO sample but intensity enhances due to the effect of Mn doping. It evidences that ion irradiation induces a microscopic structural disorder and gives rise to local distortions in the lattice. The Raman mode at 434.89 cm^{-1} reveals the vibration of the oxygen atoms in the ZnO lattice. The 527.61 cm^{-1} mode was observed, which belongs to the 2B_1 low mode, for the B-modes. In contrast, one sublattice is essentially at rest, while in the other sublattice, the neighboring atoms move in opposite directions. In the case of the B_1 (low) mode, the heavier Zn sublattice is distorted, while the B_1 (high) involves the lighter O sublattice; no net polarization is induced by the B modes, thus, the A and B modes may be classified as one polar and two non-polar modes.

After Ni^{7+} SHI irradiation, the 5% Mn doped ZnO thin film showed drastic changes in intensity, as well as wavelength of the Raman mode. In the irradiated sample, the 568.56 cm^{-1} peak disappeared after irradiation at a fluence of 1×10^{13} ions per cm^2 . It was observed that the Mn content doped in the ZnO thin films decreased the wavelength, but after SHI irradiation, it was increased, due to the effect of cascade formation in the materials. When high energetic ions were passed through the samples latent tracks were formed owing to the rearrangement of the electron positions. These latent tracks are responsible to change the internal structure of the samples. After SHI irradiation of pure and 5% Mn doped ZnO thin films, a shift in the Raman mode towards the higher wavelength was observed, due to the effect of SHI irradiation.

I-V measurements

Electrical properties of all films, *i.e.*, pristine and irradiated films, were studied by measuring current as the function of voltage. The plots are shown in Fig. 6. S. P. Pandey⁵⁹ reported an increase in the resistivity after irradiation, but in our case, the pristine and irradiated Mn doped ZnO samples revealed an enhancement in the conductivity after SHI irradiation. Hence, one could assume that the decrease in resistivity might be due to the creation of oxygen vacancies (V_O) and interstitial zinc (Zn), during the irradiation with swift heavy ions. A decrease in resistivity was observed, which could be attributed to the beginning of the hopping conduction of ion beams, producing defects. The conductivity is mainly controlled by the counter-balance between the presence of oxygen vacancies, which act as doubly charged electron donors and structural (Zn) defects,

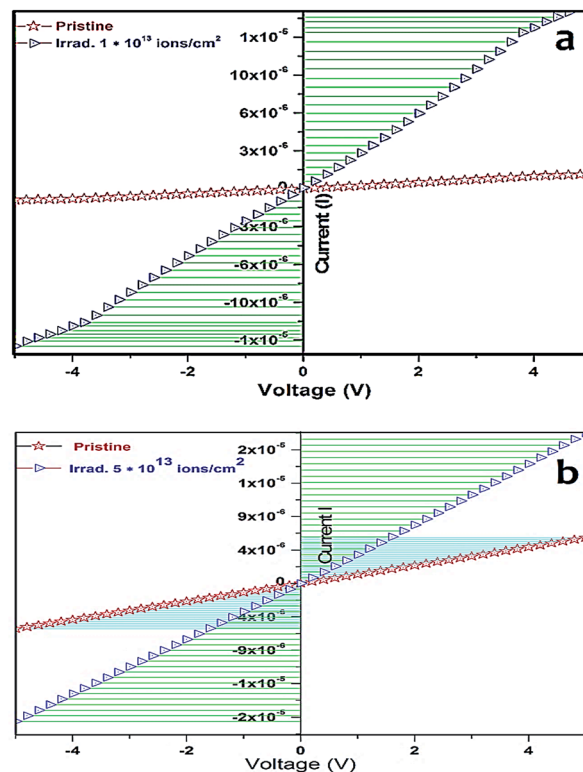


Fig. 6 I - V characteristics of (a) pristine pure and 5% Mn doped ZnO, (b) irradiated pure and 5% Mn doped ZnO thin films.

which influence the carrier mobility within the thin film. The same trend was observed for the 5% Mn doped ZnO sample. The pristine 5% Mn doped ZnO sample had increased conductivity as compared to the pure ZnO thin film, but after SHI irradiation it was drastically enhanced to 2×10^{-6} amperes. This provides evidence that the effect of SHI irradiation changes the conductivity, due to the irradiation-induced thermal annealing of the defects and hence an improvement in the crystallinity at the interface of the Mn doped ZnO thin film. The irradiation induced increment in electrical conductivity of the zinc oxide thin film is due to the scattering of charge carriers from defects and grain boundaries, and widening of the band gap, and breaks some of the covalent bonds in the ZnO semiconductor, thus generating free electron-hole pairs. The irradiation sensing study of pristine and irradiated pure and 5% Mn doped ZnO thin film were studied by a two probe I - V measurement system. The irradiation sensor efficiency (R_e) was calculated by the following equation:⁶⁰

$$R_\text{e} = \frac{I_\text{i}}{I_\text{p}} \quad (8)$$

where R_e is the irradiation sensor efficiency, I_i is the current of the irradiated sample and I_p is the current of the pristine sample. It was observed that for pure ZnO and 5% Mn doped ZnO, the values were 1.2883 and 1.5355, respectively, indicating the effect of SHI irradiation on the efficiency of the materials.

The irradiation responsibility (R_r) was calculated by the equation⁶⁰



$$R_r = \frac{I_i - I_p}{S I_p} \quad (9)$$

where R_r is the responsibility, I_i is the current of irradiation of the thin film, I_p is the current of the pristine sample and S is the thickness of the samples, calculated to be 301 ± 5 nm. Irradiation responsibility calculated after SHI irradiation of thin films was $7.069 \mu\text{A cm}^{-2}$ for pure ZnO and $8.748 \mu\text{A cm}^{-2}$ for 5% mn doped ZnO thin films. This clearly revealed the after SHI irradiation response of the thin films in the I - V curves, due to the electron cascade formation in the sample.

AFM study

Atomic force microscopy (AFM) scans of the surfaces of these films were carried out to determine the changes in surface morphology of the films. 2D and 3D AFM images of both pristine and irradiated samples clearly outline the change in surface morphology and roughness, due to the swift heavy ion beam irradiation as shown in Fig. 7. The AFM image of the pristine

sample showed a typical three dimensional growth structure with irregular grains of nearly the same sizes and a surface roughness (RMS) of 89.96 nm.

The root-mean-square roughness (RMS) has been calculated by using the formula⁶⁰

$$R_{\text{RMS}} = \sqrt{\frac{1}{N} \sum_{i=1}^N \left[(h_i - \bar{h})^2 \right]} \quad (10)$$

where h_i represents the height value at each data point, \bar{h} represents the profile mean value of the surface, and N represents the number of data points in the analyzed profile. Thus, the standard roughness or the arithmetic average roughness height represents the arithmetic mean of the deviations in height from the profile mean value, where the profile mean value is calculated using following equation:⁶⁰

$$\bar{h} = \frac{1}{N} \sum_{i=1}^N h_i \quad (11)$$

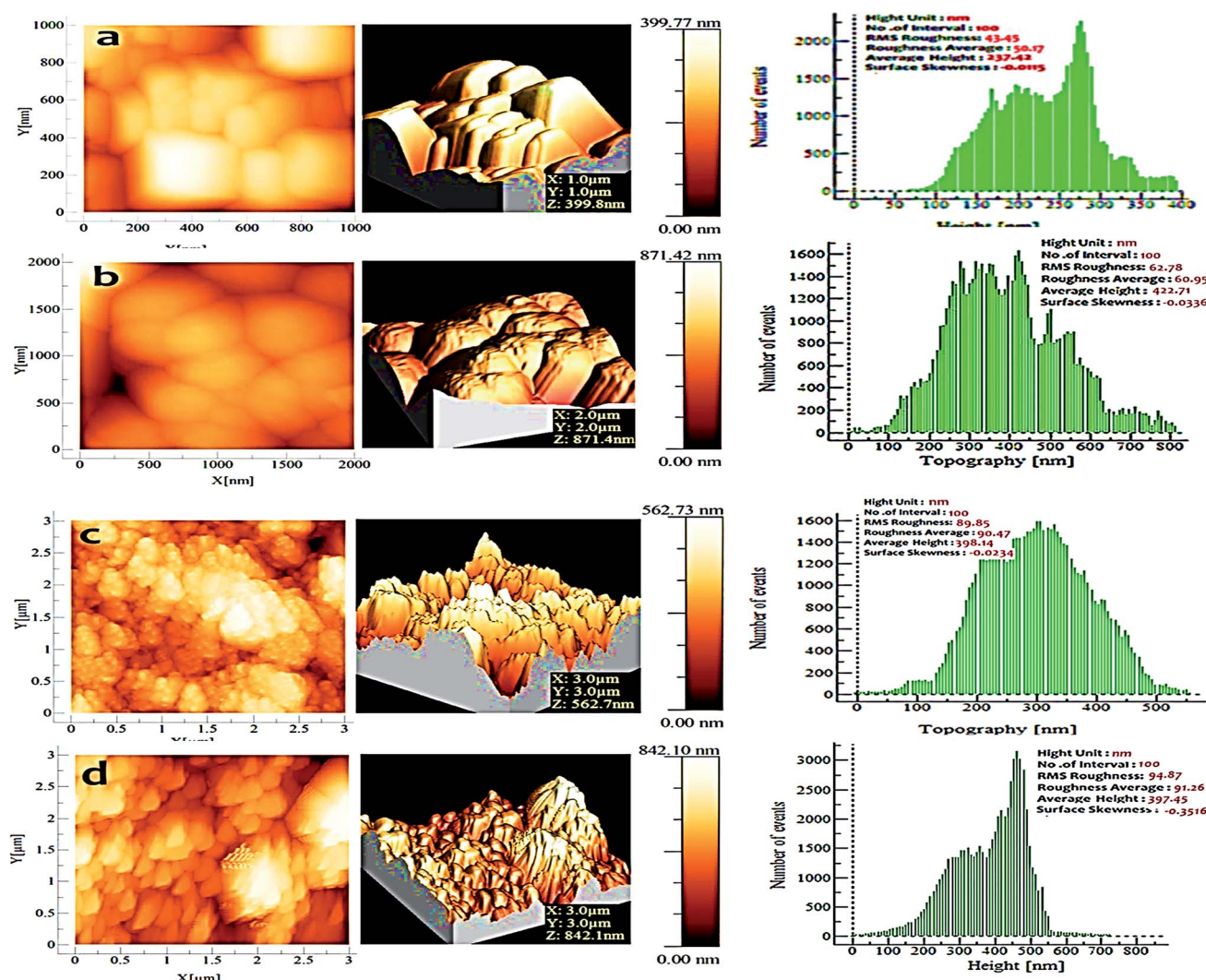


Fig. 7 AFM images of (a) pristine ZnO, (b) irradiated ZnO, (c) pristine 5% Mn doped ZnO, (d) irradiated 5% Mn doped ZnO thin films.



In comparison to pristine and irradiated ZnO, the root-mean-square (RMS) roughness of the pristine film was 43.45 nm, which increased to 62.78 nm at 1×10^{13} ions per cm^2 fluence. The same trend was observed in Mn doped ZnO samples, which increased the RMS roughness for the pristine sample to 89.85 nm, and the irradiated sample to 94.87 nm, due to the defect formation in the sample after SHI irradiation; thus, the roughness of the films is affected by the electronic excitation induced by SHI irradiation. The multiple parameters of a sample are described by factors that give information about statistical average values, the shape of the histogram heights and other extreme properties.

It was also determined that the grain size of pure and Mn doped ZnO thin films increased after the Ni^{7+} SHI irradiation.

Surface skewness was used to measure the symmetry of the variations of a surface about the mean line, and is more sensitive to occasional deep valleys or high peaks. Skewness illustrates the load carrying capacity, porosity, and characteristics of nonconventional machining processes. Negative skew is a criterion for a good bearing surface. Usually, surface skewness is used to distinguish two profiles of the same average roughness values, but of different shapes.⁶¹ For a pristine sample of pure ZnO, the surface skewness value was increased, compared to the irradiation thin film. The same results were observed for 5% Mn doped ZnO samples; the value of surface skewness was increased, due to the increase in porosity in the sample after SHI irradiation. The changes in size and shape of the grains at higher fluence are due to the high density of defects induced by the high electronic excitation energy of Ni^{7+} ion irradiation, and the major grain growth also yields an increase in the surface roughness.

Conclusions

Thin films of pure and Mn doped ZnO have been synthesized by using the dip coating technique. XRD data indicate the successful incorporation of Mn into the ZnO lattice without any secondary phase. The pristine and Mn doped ZnO thin films were irradiated by using a 160 MeV Ni^{7+} ion beam at a fluence of 1×10^{13} ions per cm^2 . The crystallite size increased after the SHI irradiation of pure and Mn doped ZnO thin films. The surface area to volume ratio and APF value were slightly decreased after SHI irradiation, due to the enhancement of voids in the samples. Photoluminescence studies revealed increased luminosity of pure and Mn doped ZnO thin films; these samples were irradiated with Ni^{7+} ions of 160 MeV energy, after which the luminosity of the samples was enhanced. The observed changes in the E_2 , high, E_2 , low and A_1 (LO) Raman modes are consistent with the creation of defects, vacancies and interstitials in the zinc and oxygen sublattices. Raman measurements revealed the appearance of forbidden modes B_1 (low) after doping 5% Mn in ZnO, due to relaxation of the Raman selection rules associated with the breakdown of translational crystal symmetry. I - V characteristics revealed that the enhancement in the conductivity after SHI irradiation was due to the ion-electron interaction. AFM data showed

a significant difference after SHI irradiation of the samples, where the film surface exhibited a higher roughness and clear grains.

Acknowledgements

The authors are grateful to IUAC, New Delhi for providing the ion beam irradiation facilities through Project No. IUAC/XIII.3A/UFR No. 52309 and Prof. S. S. Shah for his continuous encouragement.

References

- 1 B. Pelaz, S. Jaber, D. de Aberasturi, V. Wulf, T. Aida, J. de la Fuente, J. Feldmann, H. Gaub, L. Josephson, C. Kagan, N. Kotov, L. Liz-Marzán, H. MattoSSI, P. Mulvaney, C. Murray, A. Rogach, P. Weiss, I. Willner and W. Park, *ACS Nano*, 2012, **6**, 8468–8483.
- 2 A. Andrews, A. Schepartz, J. Sweedler and P. Weiss, *J. Am. Chem. Soc.*, 2014, **136**, 1–2.
- 3 P. Weiss, *ACS Nano*, 2015, **9**, 3397–3398.
- 4 C. Chey, H. Alnoor, M. Abbasi, O. Nur and M. Willander, *Phys. Status Solidi A*, 2014, **211**, 2611–2615.
- 5 S. Kumar, Y. S. Katharria, Y. Batra and D. Kanjilal, *J. Phys. D: Appl. Phys.*, 2007, **40**, 6892–6897.
- 6 P. Boisseau and B. Loubaton, *C. R. Phys.*, 2011, **12**, 620–636.
- 7 F. Adams and C. Barbante, *Spectrochim. Acta, Part B*, 2013, **86**, 3–13.
- 8 Z. Wang, *Science*, 2006, **312**, 242–246.
- 9 S. Chen, W. Chen and I. Buyanova, *Phys. Rev. B: Condens. Matter Mater. Phys.*, 2011, **83**, 245212.
- 10 C. Ronning, P. Gao, Y. Ding, Z. Wang and D. Schwen, *Appl. Phys. Lett.*, 2004, **84**, 783.
- 11 M. Willander, P. Klason, L. Yang, S. Al-Hilli, Q. Zhao and O. Nur, *Phys. Status Solidi C*, 2008, **5**, 3076–3083.
- 12 P. Solanki, A. Kaushik, V. Agrawal and B. Malhotra, *NPG Asia Mater.*, 2011, **3**, 17–24.
- 13 H. Raval and J. Gohil, *Int. J. Nucl. Desalin.*, 2010, **4**, 184.
- 14 J. Iqbal, X. Liu, A. Majid and R. Yu, *J. Supercond. Novel Magn.*, 2010, **24**, 699–704.
- 15 S. Singh, K. Barick and D. Bahadur, *J. Mater. Chem. A*, 2013, **1**, 3325.
- 16 S. F. Adams and C. Barbante, *Spectrochim. Acta, Part B*, 2013, **86**, 3–13.
- 17 M. El-Hilo and A. Dakhel, *J. Magn. Magn. Mater.*, 2011, **323**, 2202–2205.
- 18 S. Yilmaz, M. Parlak, S. Özcan, M. Altunbaş, E. McGlynn and E. Bacaksız, *Appl. Surf. Sci.*, 2011, **257**, 9293–9298.
- 19 H. Yang, C. Zhang, X. Shi, H. Hu, X. Du, Y. Fang, Y. Ma, H. Wu and S. Yang, *Biomaterials*, 2010, **31**, 3667–3673.
- 20 Y. Wang, Q. Zhao, N. Han, L. Bai, J. Li, J. Liu, E. Che, L. Hu, Q. Zhang, T. Jiang and S. Wang, *Nanomedicine: Nanotechnology, Biology and Medicine*, 2015, **11**, 313–327.
- 21 P. Boisseau and B. Loubaton, *C. R. Phys.*, 2011, **12**, 620–636.
- 22 M. Swierczewska, G. Liu, S. Lee and X. Chen, *Chem. Soc. Rev.*, 2012, **41**, 2641–2655.

23 S. Su, W. Wu, J. Gao, J. Lu and C. Fan, *J. Mater. Chem.*, 2012, **22**, 18101–18110.

24 T. Kundu, S. C. Sahoo and R. Banerjee, *Cryst. Growth Des.*, 2012, **12**, 2572–2578.

25 R. P. Singh, A. Tiwari, J. W. Choi and A. C. Pandey, *Biological approach of Zinc Oxide Nanoparticles Formation and its Characterization*, Bentham Science Publishers, 2012, vol. 3, pp. 41–50.

26 F. Santiago, K. A. Boulais, A. R. Keller, V. H. Gehman Jr and K. J. Long, *Proc. SPIE*, 2009, **7343**, 73430.

27 Y. Liu, Y. Li and H. Zeng, *J. Nanomater.*, 2013, 196521.

28 M. G. Tsoutsouva, C. N. Panagopoulos, D. Papadimitriou, I. Fasaki and M. Kompitsas, *Mater. Sci. Eng., B*, 2011, **176**, 480–483.

29 M. Smirnov, C. Baban and G. I. Rusu, *Appl. Surf. Sci.*, 2010, **256**, 2405–2408.

30 F. E. Ghodsi and H. Absalan, *Acta Phys. Pol., A*, 2010, **118**, 120–129.

31 J. G. Lu, T. Kawaharamura, H. Nishinaka, Y. Kamada, T. Ohshima and S. Fujita, *J. Appl. Phys.*, 2007, **229**, 1–10.

32 W. Gao and Z. Li, *Ceram. Int.*, 2011, **30**(7), 1155–1159.

33 M. Smirnov, C. Baban and G. I. Rusu, *Appl. Surf. Sci.*, 2010, **256**, 2405–2408.

34 S. Hasim, M. Hamid, R. Shamsudin and A. Jalar, *J. Phys. Chem. Solids*, 2009, **70**, 1501–1504.

35 D. Wu, Z. Huang, G. Yin, Y. Yao, X. Liao, D. Han, X. Huang and J. Gu, *CrystEngComm*, 2010, **12**, 192–198.

36 A. Bauer, M. Godon, J. Carlier, Q. Ma and R. H. Tipping, Absorption by H₂O and H₂O-N₂ mixtures at 153 GHz, *J. Quant. Spectrosc. Radiat. Transfer*, 1993, **50**(5), 463–475.

37 J. S. Dunlop, D. H. Hughes, S. Rawlings, S. A. Eales and M. J. Ward, *Nature*, 1994, **370**, 347–349.

38 V. Sisodia and I. Jain, *Bull. Mater. Sci.*, 2004, **27**, 393.

39 S. K. Neogi, S. Chattopadhyay, A. Banerjee, S. Bandyopadhyay, A. Sarkar and R. Kumar, *J. Phys.: Condens. Matter*, 2011, **23**, 205801.

40 H. Khawal, U. Gawai, K. Asokan and B. Dole, *RSC Adv.*, 2016, **6**, 49068–49075.

41 K. Jacob, S. Raj and L. Rannesh, *Int. J. Mater. Res.*, 2007, **98**, 776–779.

42 H. A. Khawal, N. D. Raskar, U. P. Gawai and B. N. Dole, *AIP Conf. Proc.*, 2016, 20431.

43 S. Som, S. Das, S. Dutta, M. Pandey, R. Dubey, H. Visser, S. Sharma and S. Lochab, *J. Mater. Sci.*, 2015, **51**, 1278–1291.

44 A. Sahai and N. Goswami, *Phys. E*, 2014, **58**, 130–137.

45 H. A. Khawal, U. P. Gawai, M. R. Bodke, K. Asokan and B. N. Dole, *Bionano Frontier*, 2015, **8**(3), 129–131.

46 A. Reshak, J. Ebothe, A. Wojciechowski, W. Kuznik and A. Popeda, *Physica E: Low-dimensional Systems and Nanostructures*, 2010, **42**, 1769–1771.

47 V. Mote, J. Dargad, Y. Purushotham and B. Dole, *Ceram. Int.*, 2015, **41**, 15153–15161.

48 V. Mote and B. Dole, *Adv. Mater. Res.*, 2013, **678**, 234–238.

49 Y. Hao, S. Lou, S. Zhou, R. Yuan, G. Zhu and N. Li, *Nanoscale Res. Lett.*, 2012, **7**, 100.

50 S. Sharma, R. Vyas, S. Shrivastava and Y. Vijay, *Phys. B*, 2011, **406**, 3230–3233.

51 H. Wang, G. Wang, L. Jia, C. Tang and G. Li, *J. Phys. D: Appl. Phys.*, 2007, **40**, 6549–6553.

52 J. Kang, H. Kang, S. Pang, E. Shim and S. Lee, *Thin Solid Films*, 2003, **443**, 5–8.

53 M. Koyano, P. QuocBao, L. ThanhBinh, L. HongHa, N. NgocLong and S. Katayama, *Phys. Status Solidi A*, 2002, **193**, 125–131.

54 L. Duan, G. Rao, Y. Wang, J. Yu and T. Wang, *J. Appl. Phys.*, 2008, **104**, 013909.

55 X. Zhu, H. Wu, D. Qiu, Z. Yuan, G. Jin, J. Kong and W. Shen, *Opt. Commun.*, 2010, **283**, 2695–2699.

56 S. Kumar, K. Asokan, R. Singh, S. Chatterjee, D. Kanjilal and A. Ghosh, *RSC Adv.*, 2014, **4**, 62123–62131.

57 O. Lupon, L. Chow, L. Ono, B. Cuenya, G. Chai, H. Khallaf, S. Park and A. Schulte, *J. Phys. Chem. C*, 2010, **114**, 12401–12408.

58 B. Kharroubi, R. Baghdad, A. Abdiche, M. Bousmaha, M. Bousquet, A. Zeinert, M. El Marssi, K. Zellama and S. Hamzaoui, *Phys. Scr.*, 2012, **86**, 015805.

59 S. P. Pandey, *Am. J. Mater. Sci. Technol.*, 2012, **2**(6), 215–220.

60 A. Srivastava and J. Kumar, *AIP Adv.*, 2011, **1**, 032153.

61 M. Ulmeanu, A. Serghei, I. Mihailescu, P. Budau and M. Enachescu, *Appl. Surf. Sci.*, 2000, **165**, 109–115.

